

Research Article

Channel Measurement for Multiple Frequency Bands in Subway Tunnel Scenario

Zhuomin Hu ¹, Wenli Ji,² Hengkai Zhao ¹, Xuping Zhai,¹ Asad Saleem ³,
and Guoxin Zheng ¹

¹Key Laboratory of Specialty Fiber Optics and Optical Access Networks,
Joiny International Research Laboratory of Specialty Fiber Optics and Advanced Communication, Shanghai University,
Shanghai 200444, China

²System Integration Department, Technical Center, Shanghai Shentong Metro Group Co.,Ltd, Shanghai 201103, China

³Guangdong Engineering Research Center of Base Station Antennas and Propagation,
Key Laboratory of Antennas and Propagation, Shenzhen University, Shenzhen 518000, China

Correspondence should be addressed to Hengkai Zhao; zhaohk@shu.edu.cn

Received 9 March 2021; Accepted 18 May 2021; Published 3 June 2021

Academic Editor: Renato Cicchetti

Copyright © 2021 Zhuomin Hu et al. This is an open access article distributed under the Creative Commons Attribution License, which permits unrestricted use, distribution, and reproduction in any medium, provided the original work is properly cited.

In next-generation radio communication systems, the use of higher frequency bands and the massive multiple-input-multiple-output (MIMO) systems has turned into hot research topics because they have the potential to increase network capacity significantly by exploiting the available narrowband and broadband spectrums. Therefore, the narrowband channel measurements are executed at the following five potential frequency bands, including 2.6 GHz, 3.5 GHz, 5.6 GHz, 10 GHz, and 28 GHz in the Shanghai subway tunnel environment in order to fulfill the latest standards of fifth generation (5G). Moreover, in the broadband channel measurements, the center frequency is 3.5 GHz and 5.6 GHz and the bandwidth is considered as 160 MHz, respectively. At the transmitter (Tx) side, a uniform rectangular antenna array composed of 32 elements is fixed on the platform near the tunnel walls. The receiver (Rx) is equipped with a uniform cylindrical antenna array consisting of 64 elements, which is set on a trolley along the track. Based on the acquired massive MIMO channel impulse responses, delay spread, angle spread, eigenvalue and channel capacity are analyzed. The results reveal that the multipath delay in the tunnel scenario is quite short, the delay spread and angle spread drop rapidly as the distance between Tx and Rx increases and the channel matrix gradually becomes serious. This research provides a reference for the deployment of future 5G systems in the subway tunnel.

1. Introduction

In recent years, in order to ensure the safety and efficiency of train operations, it is necessary to transmit data such as ultra-high-definition video stream monitoring, train operation control, and on-board sensing at a high rate and high reliability between train and ground, which has created an urgent need for the application and deployment of 5G in subway communications. The characteristics of the wireless propagation channel determine the final performance of the wireless communication system. Therefore, it is very important to detect the actual performance of wireless propagation channels in a real tunnel environment. So far, a large

number of channel measurements [1–14] have been carried out in different subway tunnel environments. The pioneering paper [1] shows that multiple reflections on the tunnel wall and changes in tunnel cross-section result in a relatively high diversity of MIMO channels in the tunnel environment. According to the modal theory [2], the tunnel can be regarded as a lossy waveguide, and the number of active modes decreases rapidly as the Tx-Rx distance increases, which limits the degree of freedom of the MIMO channel matrix. However, compared with single-input-single-output (SISO) channel, the improvement in channel capacity is significant. On the basis of channel measurements in a subway tunnel, the influence of polarization diversity,

space diversity, and cross section of the tunnel on the capacity of MIMO channel capacity is considered in [3–6], which provides suggestions for the design of the MIMO system in tunnel scenario. It is pointed out that the increment of the cross-sectional area improves the MIMO channel performance through measurements conducted in a two-section tunnel-like environment in [7]. In [8–10], the first keyhole measurement was introduced in the train-to-ground communication system to evaluate the keyhole probability of different polarization combinations and tunnel cross sections, and it reveals that the impact of the keyhole effect is limited. Broadband measurements are conducted in the tunnel environment in [11–13]. The influence of train cars on the wireless channel in the tunnel is considered and examined in [14, 15]. Massive MIMO channels are measured in various scenarios strongly related to the subway tunnel environments, such as subway platform halls at 6 GHz and 11 GHz [16, 17] and intrawagon environment at the millimeter wave (mmWave) bands [18]. It is proved that sum-rate capacity increases with the increase of frequency. In [19, 20], the scholars divide the tunnel into different propagation zones and propose a propagation model that covers different propagation mechanisms in the tunnel. In [21], a vector parabolic equation (VPE) field prediction model is proposed, which can be used to analyze radio propagation in railway rectangular tunnels. On the basis of [21], VPE modeling has been improved and tunnel roughness is incorporated as a parameter in [22], which can be further used for various tunnel geometries with arbitrary cross sections and curvature variations. A fast and accurate radio wave propagation modeling combining the hybrid VPE and waveguide mode theory is proposed in [23]. However, to the best of the authors' knowledge, the current MIMO antenna system used for channel measurements in real tunnel scenarios does not exceed 4×4 and the research on the long-distance train-to-ground communication system in actual subway tunnel scenarios is particularly lacking. Therefore, it is difficult to provide engineering guidance for the design of 5G systems in tunnel environments.

In this paper, we conduct narrowband and broadband wireless communication measurements in Shanghai Metro. In the narrowband measurements, five potential frequency bands of 5G, including 2.6 GHz, 3.5 GHz, 5.6 GHz, 10 GHz, and 28 GHz, are selected, and the propagation characteristics of signals in the tunnel environment are investigated. In the broadband measurements, the center frequency of the carrier is 3.5 GHz and 5.6 GHz, and the bandwidth is deliberated as 160 MHz. The Tx and Rx antenna arrays are composed of 32 and 64 elements, respectively. In order to simulate the actual wireless communications in a subway tunnel, the transmitter is fixed on the platform close to the tunnel wall, and the receiver is placed in a trolley that can move along the track. Based on the collected data, we modeled the path loss parameters and analyzed the power delay profile (PDP), root-mean-square delay spread (RMS-DS), root-mean-square angle spread (RMS-AS), eigenvalue, and channel capacity.

The rest of this paper is organized as follows. In Section 2, the environment and system for narrowband and

broadband channel measurements are introduced. Section 3 shows the fitted path loss models in narrowband measurements. In Section 4, the broadband channel parameters including PDP, RMS-DS, RMS-AS, eigenvalue, and capacity are analyzed, whereas Section 5 draws conclusions.

2. Channel Measurements

2.1. Measurement Environment Description. As depicted in Figure 1(a), the measurements were conducted in a metro Line 7 between Shanghai University and QiHua Rd. in Shanghai, China. The cross section of the tunnel is arched, with a radius of 2.78 m, a height of 5 m, and a width of 3.4 m at the bottom, as given in Figure 1(b). The tunnel wall materials are reinforced with concrete material. As shown in Figure 1(c), the tunnel can be divided into three sections structurally, S1 is a short straight tunnel with a length of 20 m, S2 is a curve with a length of 100 m and a radius of curvature of 1500 m, and S3 is a long straight tunnel with a length of 700 m. In our narrowband measurements, the farthest measurement distance between Tx and Rx is 800 m. In wideband measurements, due to the busy schedule of the subway line, we only measured the first 500 m broadband channels. Within this 500 m measurement range, 91 measurement points are sampled at 3.5 GHz, while 43 measurement points are sampled at 5.6 GHz.

As shown in Figure 2, to simulate the actual base station, the Tx is fixed at the end of the extension section of the platform, close to the tunnel wall. The Tx is 1.8 m high, and the platform height is calculated as 1.3 m, where the Rx is located on a mobile trolley on the central rail of the tunnel, simulating as an access point. In order to reduce the interference of testers on signal transmission, we increased the height of the Rx to 2.7 m.

2.2. Narrowband Measurement System. In the narrowband measurements, as shown in Figure 3, the signal generator Agilent E8257D and spectrum analyzer Ceyear 4024G are separately employed in both sides of Tx and Rx, respectively. Ultra-wideband (1 GHz - 40 GHz) omnidirectional antennas are equipped on both sides, and high-precision rubidium clocks are used to ensure synchronization. An uninterruptible power supply (UPS) ensures the power supply of the equipment in the whole measurement process. Five potential 5G frequency bands are investigated in our narrowband measurements, including 2.6 GHz, 3.5 GHz, 5.6 GHz, 10 GHz, and 28 GHz.

2.3. Broadband Measurement System. In the broadband measurements, the pseudo-noise (PN) sequence correlation method is used. At the Tx side, a PN sequence is modulated with a bandwidth of 160 MHz and a length of 1023 chips on the carrier frequencies of 3.5 GHz and 5.6 GHz by Binary Phase Shift Keying (BPSK). The Rx is divided into 8 channels to collect data in parallel. We use a low-noise amplifier to improve the received signal-to-noise ratio (SNR). Note that it takes only 10 ms to complete the static channel measurements of 2048 (32×64) subchannels in one cycle, and

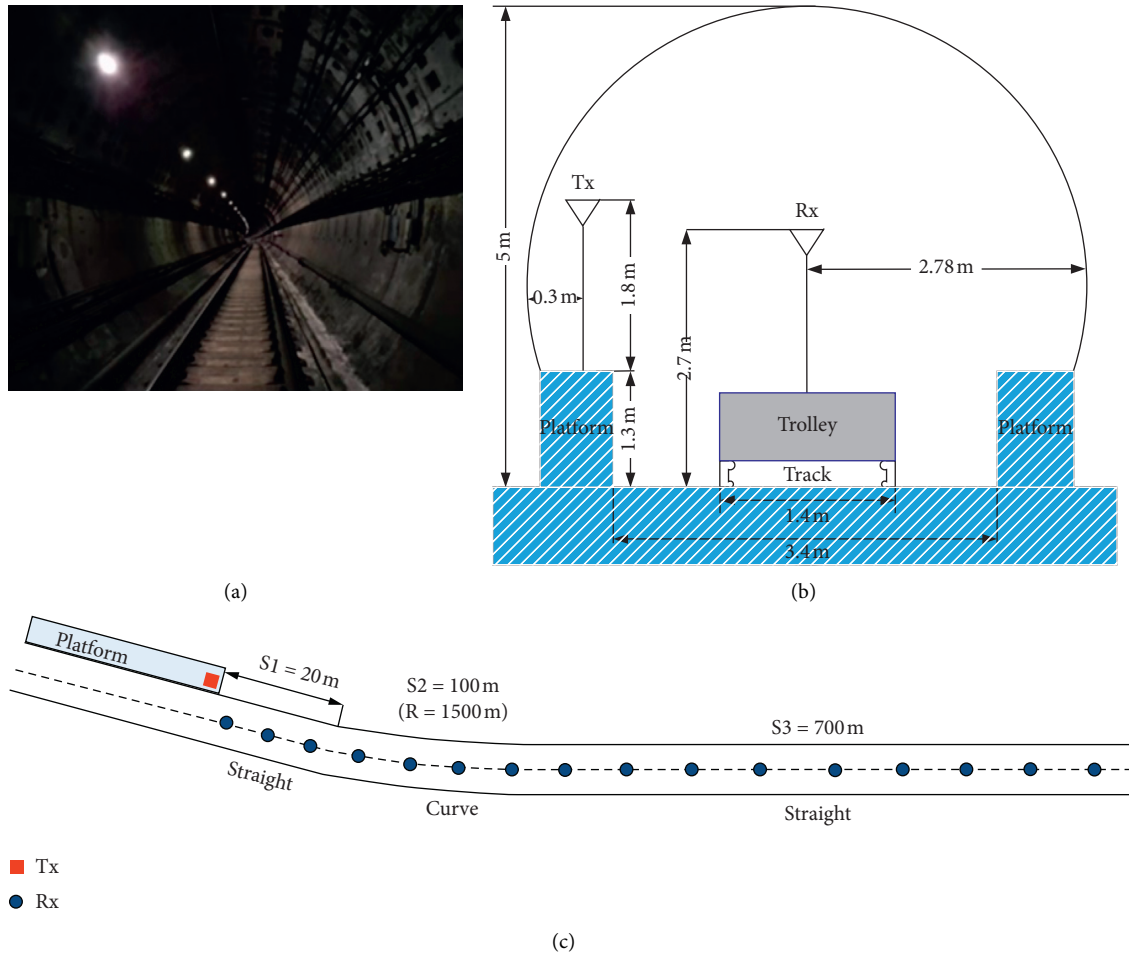


FIGURE 1: Measurement environment. (a) Real scene. (b) Cross section. (c) Floor map.



FIGURE 2: Real measurement scenario. (a) Tx side. (b) Rx side.

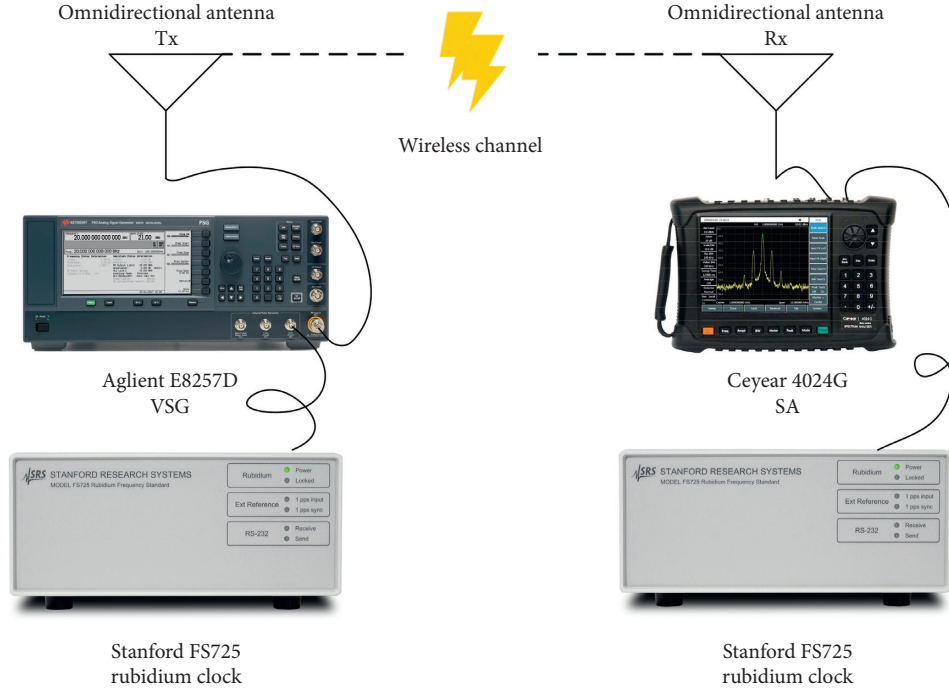


FIGURE 3: Narrowband measurements setup description.

128 cycles of data are collected at each Rx measurement position.

In the broadband measurements, directional patch antenna arrays are equipped at both Tx and Rx sides. The 3 dB beamwidth of elements on the vertical and horizontal planes is 100° and 120° , respectively. All multipath signal propagation paths in the tunnel environment can be detected perfectly. The structure of the Tx and Rx antenna is very similar to that used in [24, 25], as shown in Figure 4. The Tx is equipped with a 2×8 uniform rectangular antenna patch array. On the Rx side, the uniform cylindrical array can be divided into 8 sectors, and each sector has 4 antenna patches arranged in the vertical direction. The antenna patch spacing is half of the wavelength, and each antenna pair includes a pair of colocated dual-polarized antennas. Each patch antenna encompasses two elements with the main polarization of $\pm 45^\circ$ at 3.5 GHz and vertical and horizontal at 5.6 GHz. The important measurement parameters are summarized in Table 1.

3. Narrowband Channel Characterization

3.1. Path Loss. Path loss characterizes the signal energy attenuation after the propagation of transmitted signals. Figure 5 presents the path loss measured in the given subway tunnel environment. The most typical path loss model is first used to quantitatively analyze the path loss parameters [26]:

$$PL[dB] = PL(d_0) + 10n \log_{10} \left(\frac{d}{d_0} \right) + X_\sigma, \quad (1)$$

where d_0 is a reference distance and usually set to 1 m in a tunnel scene, d is the distance between the Tx and Rx, and n is the path loss index and equals to 2 in free space. X_σ is a

random variable with zero mean Gaussian distribution and the standard deviation is σ . $PL(d_0)$ is optimized with the path loss index n to minimize the mean-square error (MSE) between model and the real measurements. The extracted parameters are listed in Table 2. It can be found that the path loss exponent at all measured frequency bands in the tunnel is smaller than that of a free space channel and decreases with the increment of signal frequency. This is because the waveguide effect in the tunnel still exists on the whole. Furthermore, the shorter the wavelength of the signal, the greater the possibility of specular reflection on the tunnel, which enhances the waveguide effect of the tunnel on higher frequency signals.

Meanwhile, it is worth noting that the line-of-sight (LOS) propagation can be blocked by the curved tunnel wall (S2); thus, the location where the LOS components are blocked is very important to accurately predict the path loss over there [27]. Based on the geometric representation of the location for break point as shown in Figure 6, we estimate that the break point d_{bp} of LOS and non-line-of-sight (NLOS) propagation of the tunnel in this article is about 91 m. The two-slope path loss model under the tunnel can be defined as

$$PL[dB] = \begin{cases} PL(d_0) + 10n_1 \log_{10} \left(\frac{d}{d_0} \right) + X_{\sigma_1}, & d \leq d_{bp}, \\ PL(d_{bp}) + 10n_2 \log_{10} \left(\frac{d}{d_{bp}} \right) + X_{\sigma_2}, & d > d_{bp}. \end{cases} \quad (2)$$

Figure 7 shows the two-slope path loss model at 28 GHz. The coefficients of the models for all frequency bands are

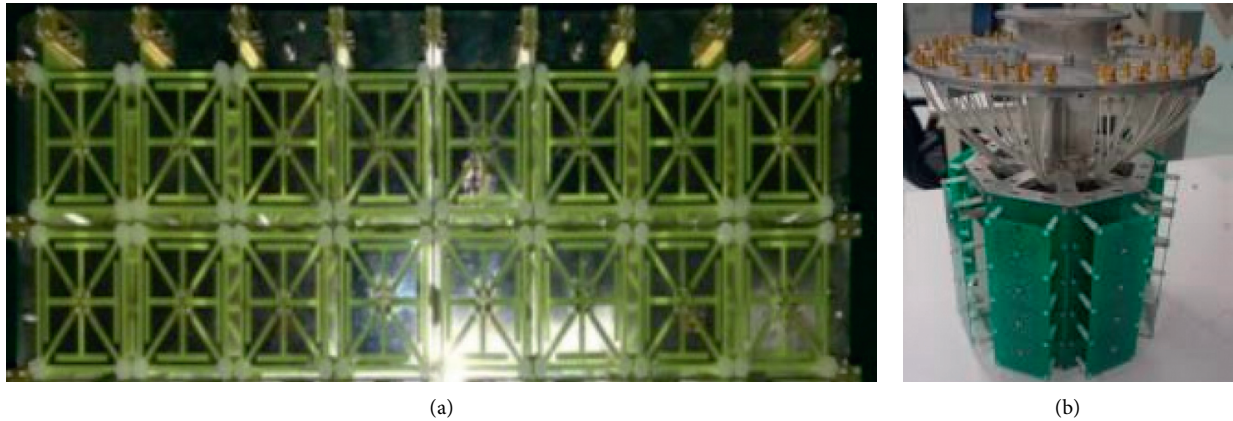


FIGURE 4: Antenna array used in the measurements. (a) Tx. (b) Rx.

TABLE 1: Measurement parameters.

Parameters	Narrowband measurement		Broadband measurement	
Frequency	2.6 GHz/3.5 GHz/5.6 GHz/10 GHz/28 GHz		3.5 GHz/5.6 GHz	
Probe signal	Sine wave		PN sequence	
Bandwidth	0		160 MHz	
Antenna structure	Omnidirectional antenna (Tx)	Omnidirectional antenna (Rx)	Uniform rectangular array (Tx)	Uniform cylindrical array (Rx)
Polarization of Tx/Rx antenna	Vertical/vertical		Dual polarization: 3.5 GHz: $\pm 45^\circ$ 5.6 GHz: vertical and horizontal	
Height of Tx/Rx antenna	1.8 m/2.7 m		1.8 m/2.7 m	
Farthest measurement distance	800 m		500 m	
Number of sampling points	85		3.5 GHz: 91 5.6 GHz: 43	

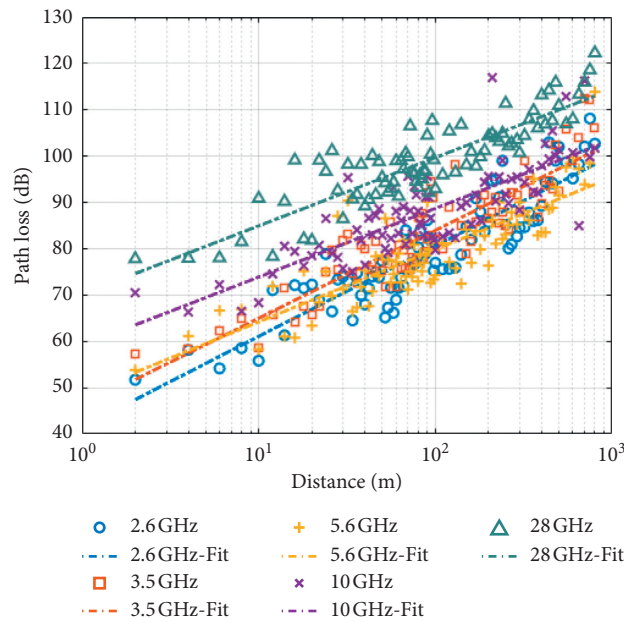


FIGURE 5: Path loss at different frequencies.

TABLE 2: Path loss coefficients.

Frequency (GHz)	$PL(d_0)$ (dB)	n	σ (dB)
2.6	41.55	1.95	5.18
3.5	46.01	1.90	5.06
5.6	48.59	1.56	5.63
10	59.07	1.48	5.85
28	70.19	1.47	4.53

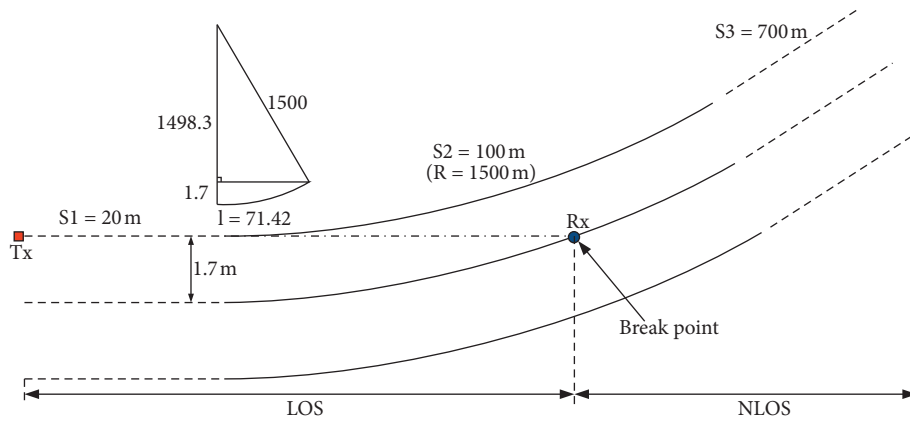


FIGURE 6: The location for break point.

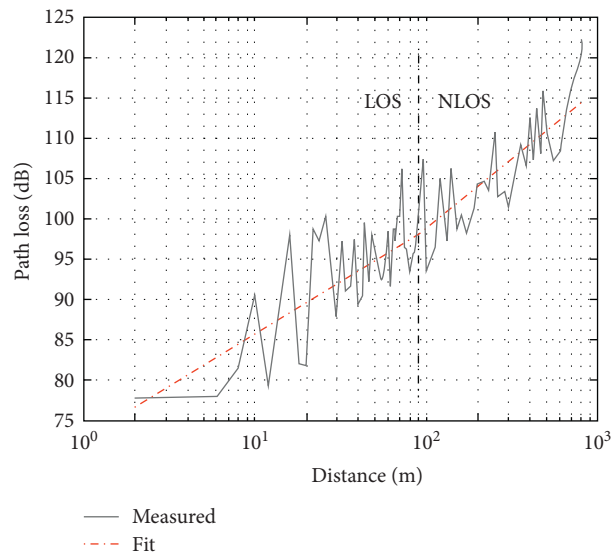


FIGURE 7: Measured data versus two-slope path loss model at 28 GHz.

listed in Table 3. The path loss exponent varies from 1.06 to 1.80 in the LOS propagation scenario, while in the NLOS scenario, the path loss exponent ranges from 1.67 to 2.42. This shows that before the break point, the multipath propagates in the axial direction of the tunnel and propagates in the way of reflection between the tunnel walls, resulting in a smaller propagation loss. When the curved tunnel wall occludes the multipath components, the above waveguide effect is weakened. Compared with the path loss

models in [27], it shows a smaller path loss exponent in the NLOS area mainly because the radius of curvature of 1500 m is much larger than that in [27]. In addition, Tx is placed close to the tunnel wall in our measurements, while Tx and Rx in [27] are set in the center of a tunnel. From the comparison of 5 measured signal frequencies, the propagation attenuation rate of 5.6 GHz is the smallest in the LOS scenario while the path loss exponents of 10 GHz and 28 GHz are smaller in the NLOS scenario.

TABLE 3: Path loss coefficients of two-slope models.

Frequency (GHz)	LOS			NLOS		
	$PL(d_0)$ (dB)	n_1	σ_1 (dB)	$PL(d_{bp})$ (dB)	n_2	σ_2 (dB)
2.6	47.17	1.57	4.75	77.85	2.42	5.27
3.5	47.29	1.80	4.20	82.46	2.09	5.87
5.6	56.20	1.06	5.89	76.92	2.09	4.82
10	59.90	1.41	4.75	87.45	1.67	6.77
28	72.90	1.29	4.83	98.11	1.72	4.06

4. Broadband Channel Characterization

4.1. PDP and RMS-DS. PDP is frequently used to characterize the distribution characteristics of multipaths in the delay domain. Average Power Delay Spectrum (APDP) is the average of PDPs over all Tx-Rx links, which can reduce the interference of small-scale fading on effective signal multipaths [28], expressed as

$$\text{APDP}(\tau) = \frac{1}{N_T N_R} \sum_{m=1}^{N_T} \sum_{n=1}^{N_R} |h_{mn}(\tau)|^2, \quad (3)$$

where N_T and N_R represent the number of array elements of Tx and Rx, respectively. $h_{mn}(\tau)$ is the complex channel impulse response between the m -th Tx and the n -th Rx.

Figure 8 shows normalized APDP at all measurement points in the tunnel scenario. Taking APDP at 3.5 GHz as an example, the multipath component decays very quickly with time. If -20 dB is chosen as the power threshold of the multipath components, the delay of the multipath component will rapidly attenuate from 100 ns to 50 ns with the increase of Tx-Rx distance. The trend of APDP at 5.6 GHz is observed roughly the same as that of 3.5 GHz.

We can further study the delay spread by APDP. Delay spread is a statistical description of the delay characteristics of a multipath channel, which determines the highest transmission rate supported by the channel, in case of no intersymbol interference within a broadband communication system. RMS-DS is usually defined as the central second moment of APDP, expressed as follows [26]:

$$\tau_{rms} = \sqrt{\frac{\sum_{k=1}^K P(\tau_k) \cdot (\tau_k)^2}{\sum_{k=1}^K P(\tau_k)} - \left(\frac{\sum_{k=1}^K P(\tau_k) \cdot (\tau_k)}{\sum_{k=1}^K P(\tau_k)} \right)^2}, \quad (4)$$

where K represents the number of effective multipath components. $P(\tau_k)$ and τ_k are the estimated power and the relative delay of the k -th effective multipath.

It is observed from Figure 9(a) that RMS-DS decreases with the increase of Tx-Rx distance, which is basically consistent with the simulation results of the ray-tracing method in [15]. This can be explained by the modal theory [29]. When Tx-Rx distance is short, multiple propagation modes are excited. As the distance increases, especially after entering the NLOS propagation scenario, the high-order modal attenuation is severe, and only the low-order basic modal is maintained. Therefore, the RMS-DS in the NLOS region is relatively stable and changes smoothly. The statistic

and percentiles are listed in Table 4. Except for the LOS scenario when the Tx-Rx distance is short, RMS-DS varies from 6 ns to 10 ns at 3.5 GHz, while RMS-DS at 5.6 GHz changes from 4 ns to 8 ns. Overall, it can be concluded from Figure 9(b) that the RMS-DS at 3.5 GHz is slightly larger than that of 5.6 GHz.

4.2. RMS-AS. RMS-AS is usually explored to indicate the expansion of the departure or arrival angle of signals on the antenna due to multipath reflection and scattering effects. In this paper, we use the Bartlett beamforming method to estimate the angle characteristics in azimuth of arrival (AOA), the elevation of arrival (EOA), azimuth of departure (AOD), and elevation of departure (EOD). RMS-AS is defined as the second-order central moment of the angle spectrum and can be calculated as follows [26]:

$$\Delta_{rms} = \sqrt{\frac{\sum_{k=1}^K (\theta_k - \bar{\theta})^2 P(\theta_k)}{\sum_{k=1}^K P(\theta_k)}}, \quad (5)$$

$$\bar{\theta} = \frac{\sum_{k=1}^K \theta_k P(\theta_k)}{\sum_{k=1}^K P(\theta_k)}, \quad (6)$$

where θ_k is the angle of the k -th effective multipath.

Figure 10 shows the angle-delay power spectrum at a typical LOS position (Tx-Rx distance of 15 m) and NLOS position (Tx-Rx distance of 400 m) in AOA. It can be observed that at a typical LOS measurement location, most of the multipaths are concentrated in the LOS (about -90°) direction, and the other multipaths can be received by Rx in the directions of -60° and -100° , reflected from the walls of both sides of the tunnel. At the NLOS location, due to the limited propagation space of the tunnel, the waveguide effect forces the multipath components to propagate along the direction of the track. The angles for approaching the receiver are basically the same, all around -80° .

It is found that the RMS-AS decreases rapidly with the increase of the Tx-Rx distance from Figure 11. The statistical results of all RMS-AS are summarized in Table 5. The uniform cylindrical array at the Rx side can receive signals from different azimuth angles of each sector, and a larger expansion of the angle of arrival can be obtained. About 90% of the AOD and EOD is less than 10° at the Tx side, and 90% of EOA is less than 5° . Comparing the RMS-AS at different frequency bands, it can be concluded that the RMS-AS at 3.5 GHz is larger than that of 5.6 GHz except in AOA. The

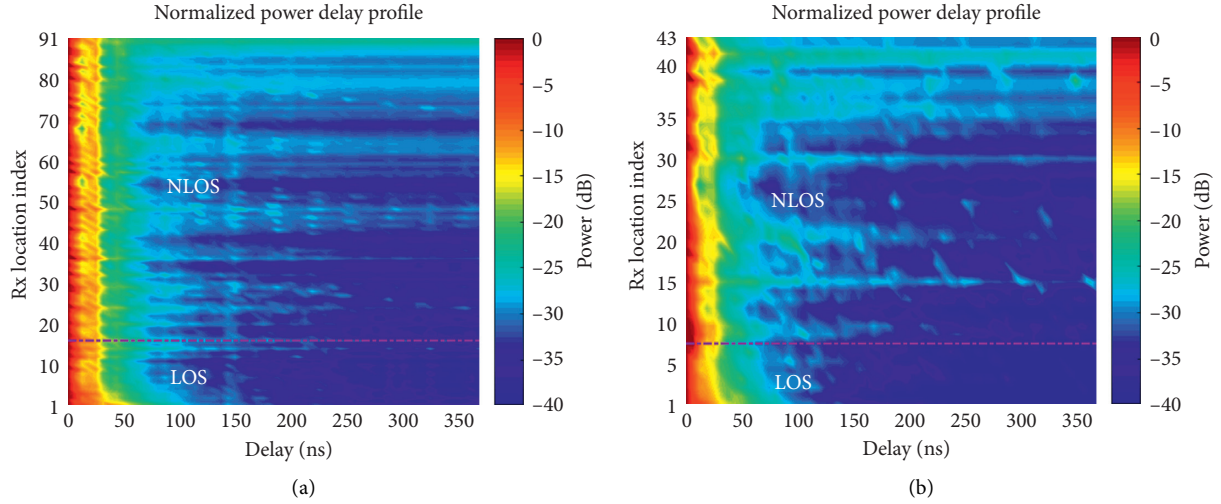


FIGURE 8: Normalized APDP. (a) 3.5 GHz. (b) 5.6 GHz.

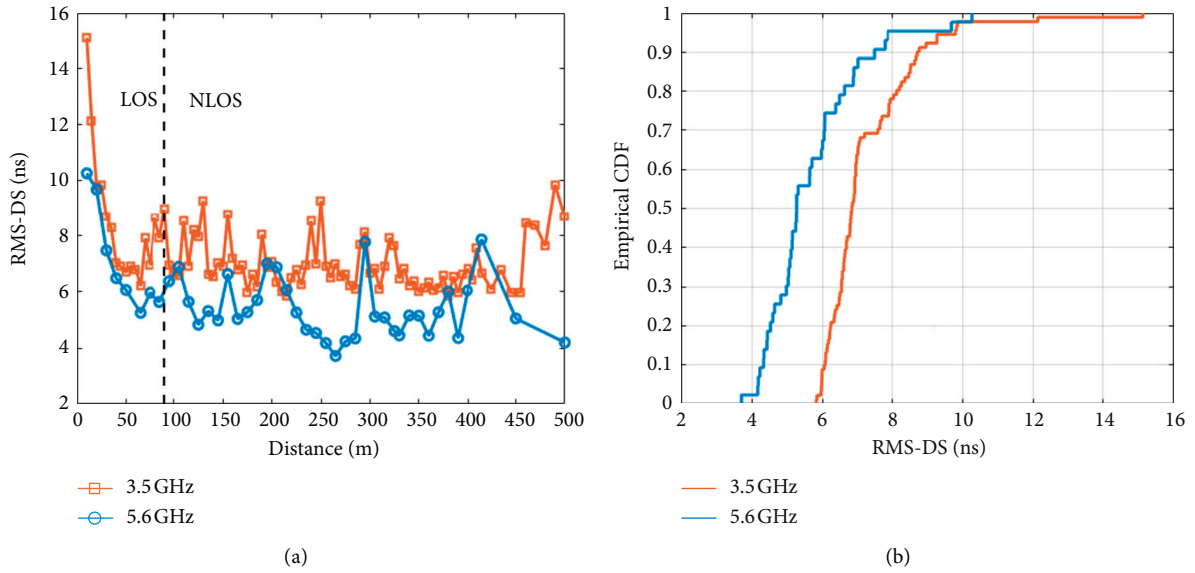


FIGURE 9: RMS-DS. (a) Variation with Tx-Rx distance. (b) CDF.

TABLE 4: Statistic of RMS-DS.

Frequency (GHz)	10% (ns)	50% (ns)	90% (ns)	Mean (ns)	Standard deviation (ns)
3.5	6.09	6.84	8.72	7.26	1.40
5.6	4.34	5.28	7.48	5.70	1.40

above experimental conclusions are quite beneficial to the deployment and design of antennas in tunnel scenarios.

4.3. *Eigenvalue and Channel Capacity.* We estimate the performance of the wireless communication system by measuring the channel capacity and the eigenvalue

distribution of the channel matrix. The complex channel matrix H can be expressed as follows:

$$H = \begin{pmatrix} \widetilde{h}_{11} & \cdots & \widetilde{h}_{1N_R} \\ \vdots & \ddots & \vdots \\ \widetilde{h}_{N_T1} & \cdots & \widetilde{h}_{N_TN_R} \end{pmatrix}, \quad (7)$$

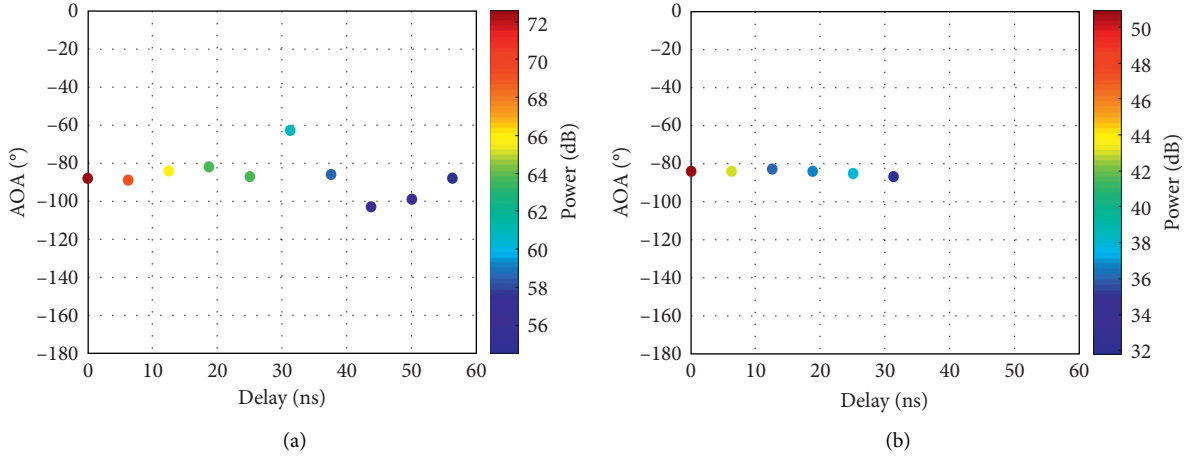


FIGURE 10: Multipath component angle-delay power spectrum at 3.5 GHz in AOA. (a) At a typical LOS position (Tx-Rx distance of 15 m). (b) At a typical NLOS position (Tx-Rx distance of 400 m).

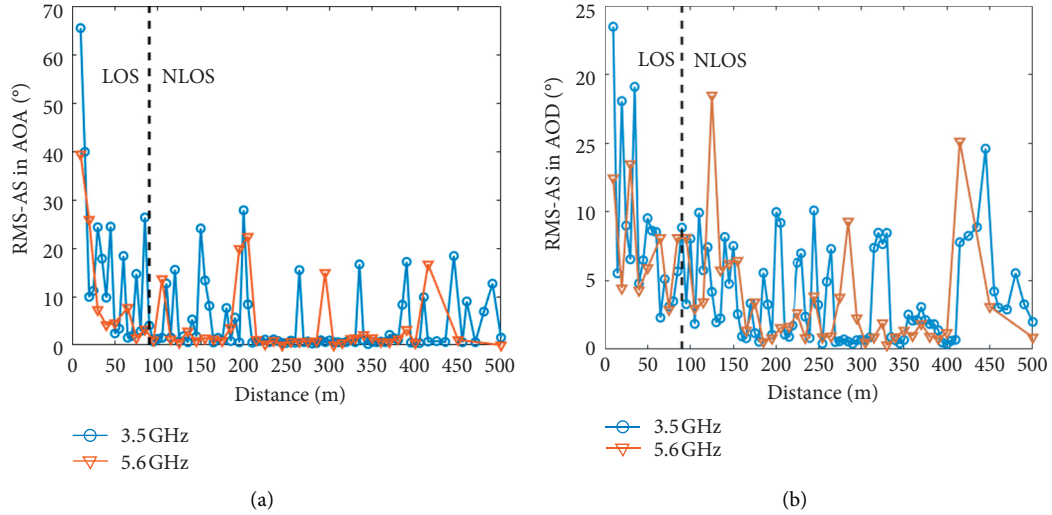


FIGURE 11: RMS-AS variation with Tx-Rx distance. (a) AOA. (b) AOD.

TABLE 5: Statistics of RMS-AS.

Frequency (GHz)	Angle	10% (°)	50% (°)	90% (°)	Mean (°)	Standard deviation (°)
3.5	AOA	0.47	1.16	17.83	6.15	9.74
	EOA	0.49	1.20	3.78	2.01	2.61
	AOD	0.56	3.08	9.00	4.48	4.35
	EOD	1.83	5.34	9.42	5.52	2.90
5.6	AOA	0.22	1.25	16.68	4.96	8.34
	EOA	0.71	1.66	4.63	2.36	1.92
	AOD	0.77	2.65	9.30	4.09	4.30
	EOD	0.11	3.63	7.61	4.11	4.46

where \widetilde{h}_{mn} can be obtained by summing the multipath signals of each subchannel:

$$\widetilde{h}_{mn} = \sum_{k=1}^K h_{mn}(\tau_k). \quad (8)$$

The normalized eigenvalue λ_i of HH^\dagger is seen in Figure 12. Here, $(\cdot)^\dagger$ is the conjugate transpose of the matrix. It can be found that the attenuation of the channel matrix eigenvalues at a typical LOS position (Tx-Rx distance of 15 m) is slower than that of NLOS position (Tx-Rx distance of 400 m). The

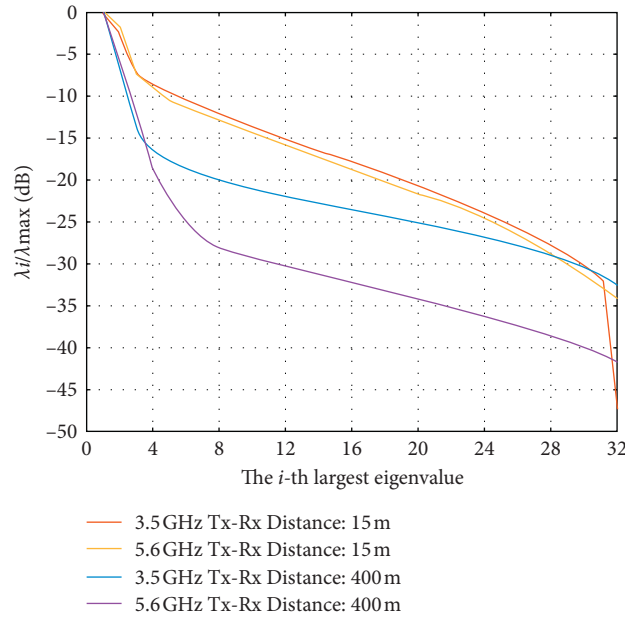


FIGURE 12: Normalized eigenvalues at a typical LOS scenario and NLOS scenario.

normalized eigenvalue of 5.6 GHz has greater attenuation than that of 3.5 GHz. Assuming that -16 dB (0.025) is used as the eigenvalue threshold, it is considered that eigenvalues that are smaller than the threshold value have little effect on the channel matrix. Taking the condition of Tx-Rx distance of 15 m at 3.5 GHz as an example, the number of effective eigenvalues of the channel matrix is only 12, which is much smaller than the minimum number of Tx and Rx antenna elements $\min(N_T, N_R)$. It shows that in the measured tunnel environment, the massive MIMO channel matrix has a serious rank reduction, which will have an adverse effect on the multistream parallel transmissions in wireless communication systems.

Channel capacity refers to the maximum information rate transmitted in an error-free channel, which is one of the most important indicators for measuring wireless propagation channels. It can be expressed as [30]

$$C = \log_2 \det \left[I_{N_R} + \frac{\rho}{N_T} H_n H_n^\dagger \right], \quad (9)$$

where I_{N_R} is the real identity matrix. ρ is the SNR at the Rx side, which is set to 10 dB here. H_n is the normalized channel matrix from which the channel complex matrix H removes the influence of path loss and satisfies $\|H_n\|_F^2 = N_T N_R$.

In order to explore the deployment prospects of massive MIMO in subway tunnel scenarios, we focus on the influence of the Tx-Rx distance and the number of transmitting antenna elements on the channel capacity. Under the condition of a constant $SNR = 10$ dB and a fixed number $N_R = 64$ of cylindrical antenna elements at the Rx side,

channel capacity at 3.5 GHz and 5.6 GHz is shown in Figures 13(a) and 13(b), respectively.

Figure 13(c) shows the 32×64 MIMO channel capacity with the Tx-Rx distance in the tunnel scenario at 3.5 GHz and 5.6 GHz. It can be seen that, under the propagation condition of LOS, the channel capacity decreases rapidly with the increase of the Tx-Rx distance. Consider the 3.5 GHz channel capacity as an example; it drops from 85 bits/s/Hz to 45 bits/s/Hz. The average channel capacities of 3.5 GHz and 5.6 GHz are 54.96 bits/s/Hz and 55.55 bits/s/Hz in the LOS propagation scenario, respectively. Channel capacity at 5.6 GHz appears to be slightly higher than that at 3.5 GHz in the LOS scenario. This can be explained as the higher the frequency is, the more modalities are excited, which enhances the decorrelation at the receiver side. When the Rx enters the NLOS area, the number of active modes decays rapidly and the channel capacity attenuates slowly. The average channel capacity of 3.5 GHz and 5.6 GHz in the NLOS area is 36.24 bits/s/Hz and 28.96 bits/s/Hz, respectively. From the ray theory point of view, in the LOS area, the direct component exists stably. As the distance between Tx and Rx increases, the distance between the multipath component reflected by the tunnel wall and the direct component gradually decreases, resulting in smaller RMS-DS and RMS-AS. The similarity between multipath components is increased, thereby reducing the ability of channel diversity gain. In the NLOS propagation area, the direct component is blocked by the tunnel curvature, and the surface of the curved tunnel wall will provide irregular reflection. The propagation distance between multipath components is relatively stable, so the channel capacity does not change significantly with the distance between Tx and

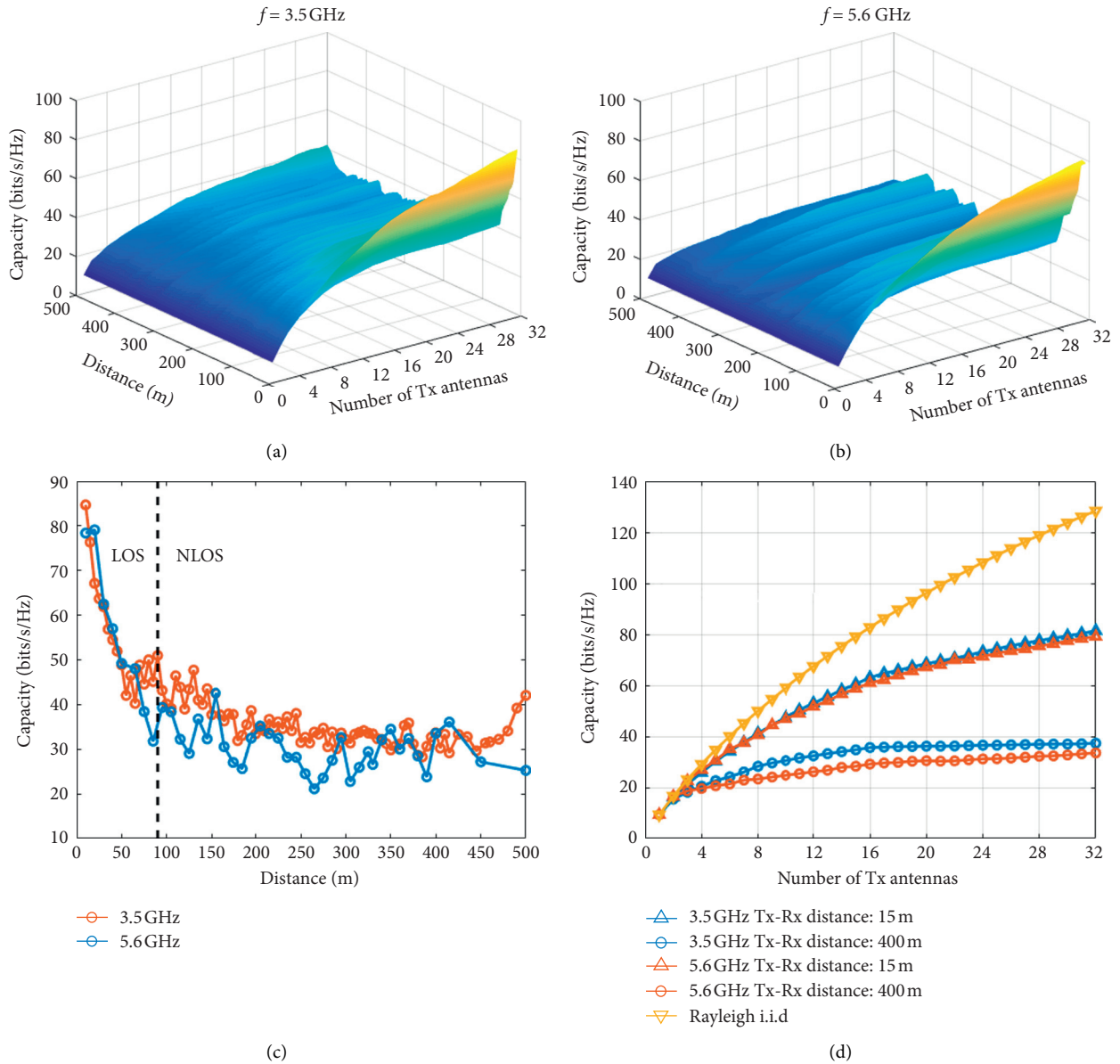


FIGURE 13: Channel capacity. (a) Channel capacity at 3.5 GHz. (b) Channel capacity at 5.6 GHz. (c) 32×64 massive MIMO channel capacity versus distance. (d) Channel capacity versus the number of Tx antenna elements.

Rx. As a reference, the 32×64 MIMO Rayleigh channel capacity is about 128 bits/s/Hz. The MIMO Rayleigh channel capacity of 4×4 , which is deployed in the current subway communication system, is about 11 bits/s/Hz. The channel capacity is considerably lower than the Rayleigh channel capacity under the condition of the same antenna scale. This is because that the tunnel measurement environment in this paper is obviously nonscattering environment, the RMS-DS and RMS-AS are quite small, and the spatial correlation is very large. In addition, the rank reduction of the channel matrix mentioned above also limits the capacity of the channel. However, compared with the 4×4 MIMO deployment in tunnels, there is still a considerable improvement in channel capacity. The channel capacity of 3.5 GHz is generally greater than 5.6 GHz in the NLOS scenario, which

is consistent with the APDP observed in Figure 8. It can be seen that the number and power of multipaths at 3.5 GHz are greater than those at 5.6 GHz in the NLOS area, which results in greater delay spread and angle spread and smaller spatial correlation.

As we all know, under the condition when antennas are not correlated with each other, the channel capacity of MIMO can increase linearly with $\min(N_T, N_R)$. It can be seen from Figure 13(d) that at the Tx-Rx distance of 400 m, the channel capacity converges rapidly as the number of Tx antenna elements increases. When the number of Tx antenna elements is larger than 16, the channel capacity remains relatively constant, and the 3.5 GHz and 5.6 GHz channel capacities are 37 bits/s/Hz and 33 bits/s/Hz, respectively. At the Tx-Rx distance of 15 m, the channel

capacity at 5.6 GHz and 3.5 GHz is relatively close. When the number of Tx antenna elements reaches 32, the channel capacity is about 80 bits/s/Hz.

5. Conclusion

In this article, we carried out narrowband measurements at five potential frequency bands, and 32×64 broadband massive MIMO channel is analyzed in the tunnel scenario of Shanghai Metro Line 7. The tunnel is divided into two propagation areas: the LOS area and the NLOS area. Path loss, PDP, RMS-DS, RMS-AS, channel matrix eigenvalue, and channel capacity have been investigated based on the acquired channel impulse response. The proposed method will have many fruitful applications for the massive MIMO channel-based 5G mobile communications in underground tunnels, mines, and railways. From this article, we can summarize the following conclusions:

- (1) The overall path loss exponent in the tunnel is smaller than that of the free space. From a comprehensive comparison of measured frequencies, it is inferred that 5.6 GHz has the smallest path loss attenuation rate in the LOS area, while 10 GHz and 28 GHz have smaller path loss exponents in the NLOS area
- (2) The waveguide effect of the tunnel limits the RMS-DS and RMS-AS of the channel. The multipath delay is within 100 ns, the maximum value of RMS-DS is less than 15 ns, and the mean value of RMS-AS is less than 6.15°. RMS-DS and RMS-AS attenuate rapidly as the Tx-Rx distance increases
- (3) In the tunnel scenario, the eigenvalue of the channel matrix decays quickly, and the channel rank reduction is serious. The measured 32×64 MIMO channel capacity at 3.5 GHz has a maximum value of 85 bits/s/Hz and a minimum value of 28 bits/s/Hz. There is a big gap with the Rayleigh channel due to the high similarity of multipath components. However, compared with the MIMO system deployed in the contemporary communication system in tunnels, the measured channel capacity has been greatly improved. In the NLOS scenario, as the number of Tx antenna elements increases, channel capacity shows a trend of rapid convergence
- (4) Through the comparison of the measured frequency bands, RMS-DS, RMS-AS, and channel capacity at 3.5 GHz are slightly larger than these at 5.6 GHz

Data Availability

The measurement data have not been made available because of intellectual property protection. Furthermore, the data are shared with our partner company and will be used in our future work.

Conflicts of Interest

The authors declare that they have no conflicts of interest.

Acknowledgments

This work was supported by the National Natural Foundation of China under Grant 61871261 and the Scientific Research Project of Shanghai Shentong Metro Group Co., Ltd. (JS-KY19R031).

References

- [1] M. Lienard, P. Degauque, J. Baudet, and D. Degardin, "Investigation on MIMO channels in subway tunnels," *IEEE Journal on Selected Areas in Communications*, vol. 21, no. 3, pp. 332–339, 2003.
- [2] J. Molina-Garcia-Pardo, M. Lienard, P. Degauque, D. G. Dudley, and L. Juan-Llaser, "Interpretation of MIMO channel characteristics in rectangular tunnels from modal theory," *IEEE Transactions on Vehicular Technology*, vol. 57, no. 3, pp. 1974–1979, 2008.
- [3] J.-M. Molina-Garcia-Pardo, M. Lienard, P. Degauque, C. Garcia-Pardo, and L. Juan-Llaser, "MIMO channel capacity with polarization diversity in arched tunnels," *IEEE Antennas and Wireless Propagation Letters*, vol. 8, pp. 1186–1189, 2009.
- [4] J. A. Valdesueiro, B. Izquierdo, and J. Romeu, "MIMO channel measurement campaign in subway tunnels," in *Proceedings of the Fourth European Conference on Antennas and Propagation (EuCAP)*, pp. 1–4, Barcelona, Spain, April 2010.
- [5] J. A. Valdesueiro, B. Izquierdo, and J. Romeu, "On 2 × 2 MIMO observable capacity in subway tunnels at S-band: an experimental approach," *IEEE Antennas and Wireless Propagation Letters*, vol. 9, pp. 1099–1102, 2010.
- [6] D. Li and J. Wang, "Effect of antenna parameters on the field coverage in tunnel environments," *International Journal of Antennas and Propagation*, vol. 2016, Article ID 8180124, 10 pages, 2016.
- [7] R. Sun, D. W. Matolak, C. Tao et al., "Investigation of MIMO channel characteristics in a two-section tunnel at 1.4725 GHz," *International Journal of Antennas and Propagation*, vol. 2017, Article ID 3693149, 12 pages, 2017.
- [8] J. Moreno García-Loygorri, L. De Haro, C. Rodríguez, L. Cuéllar, and J. M. Riera, "Influence of polarization on keyhole probability on a MIMO-OFDM train-to-wayside system on tunnels," *IEEE Antennas and Wireless Propagation Letters*, vol. 14, pp. 1798–1801, 2015.
- [9] J. Moreno, L. de Haro, C. Rodríguez, L. Cuéllar, and J. M. Riera, "Keyhole estimation of an MIMO-OFDM train-to-wayside communication system on subway tunnels," *IEEE Antennas and Wireless Propagation Letters*, vol. 14, pp. 88–91, 2015.
- [10] J. Moreno, J. M. Riera, L. de Haro et al., "MIMO keyholes on tunnels: Measurements," in *Proceedings of the European Conference on Antennas and Propagation (EuCAP)*, pp. 1–3, Davos, Switzerland, April 2016.
- [11] J. Li, Y. Zhao, J. Zhang, R. Jiang, C. Tao, and Z. Tan, "Radio channel measurements and analysis at 2.4/5GHz in subway tunnels," *China Communications*, vol. 12, no. 1, pp. 36–45, 2015.
- [12] B. Izquierdo, S. Capdevila, L. Jofre, and J. Romeu, "Evaluation of MIMO capacity in train tunnels," in *Proceedings of the IEEE Antennas and Propagation Society International Symposium*, pp. 1365–1368, Honolulu, HI, USA, June 2007.
- [13] R. He, Z. Zhong, and C. Briso, "broadband channel long delay cluster measurements and analysis at 2.4GHz in subway

- tunnels,” in *Proceedings of the IEEE 73rd Vehicular Technology Conference*, pp. 1–5, VTC Spring, Budapest, Hungary, May 2011.
- [14] E. Masson, Y. Cocheril, M. Berbineau et al., “MIMO channel characterization in subway tunnel for train-to-wayside applications,” in *Proceedings of the International Conference on ITS Telecommunications*, pp. 732–736, Taipei, Taiwan, November 2012.
- [15] T. Zhou, H. Li, R. Sun, Y. Wang, L. Liu, and C. Tao, “Simulation and analysis of propagation characteristics for tunnel train-ground communications at 1.4 and 40 GHz,” *IEEE Access*, vol. 7, pp. 105123–105131, 2019.
- [16] Q. Wang, B. Ai, R. He et al., “Measurement-based massive MIMO channel characterization in subway station,” in *Proceedings of the European Conference on Antennas and Propagation (EuCAP)*, pp. 1–5, London, UK, March 2018.
- [17] J. Li, B. Ai, R. He et al., “Channel characterization for massive MIMO in subway station environment at 6 GHz and 11 GHz,” pp. 1–5, IEEE Vehicular Technology Conference (VTC-Fall), Chicago, IL, USA, 2018.
- [18] F. Challita, V. M. Rodrigo-Peñarrocha, L. Rubio et al., “On the contribution of dense multipath components in an intrawagon environment for 5G mmW massive MIMO channels,” *IEEE Antennas and Wireless Propagation Letters*, vol. 18, no. 12, pp. 2483–2487, 2019.
- [19] K. Guan, Z. Zhong, B. Ai et al., “Complete propagation model in tunnels,” *IEEE Antennas and Wireless Propagation Letters*, vol. 12, pp. 741–744, 2013.
- [20] Y. P. Zhang, “Novel model for propagation loss prediction in tunnels,” *IEEE Transactions on Vehicular Technology*, vol. 52, no. 5, pp. 1308–1314, 2003.
- [21] P. Bernardi, D. Caratelli, R. Cicchetti, V. Schena, and O. Testa, “A numerical scheme for the solution of the vector parabolic equation governing the radio wave propagation in straight and curved rectangular tunnels,” *IEEE Transactions on Antennas and Propagation*, vol. 57, no. 10, pp. 3249–3257, 2009.
- [22] X. Zhang and C. D. Sarris, “Statistical modeling of electromagnetic wave propagation in tunnels with rough walls using the vector parabolic equation method,” *IEEE Transactions on Antennas and Propagation*, vol. 67, no. 4, pp. 2645–2654, 2019.
- [23] X. Zhang, N. Sood, and C. D. Sarris, “Fast radio-wave propagation modeling in tunnels with a hybrid vector parabolic equation/waveguide mode theory method,” *IEEE Transactions on Antennas and Propagation*, vol. 66, no. 12, pp. 6540–6551, 2018.
- [24] L. Hao, J. Rodríguez-Piñero, X. Cai et al., “Measurement-based double-directional polarimetric characterization of outdoor massive MIMO propagation channels at 3.5GHz,” in *Proceedings of the IEEE International Workshop on Signal Processing Advances in Wireless Communications (SPAWC)*, pp. 1–5, Atlanta, GA, USA, November 2020.
- [25] L. Hao, J. Rodríguez-Piñero, X. Yin, and H. Wang, “Measurement-based massive MIMO polarimetric channel characterization in outdoor environment,” *IEEE Access*, vol. 7, pp. 171285–171296, 2019.
- [26] A. Goldsmith, *Wireless Communications*, Cambridge University Press, Cambridge, UK, 2005.
- [27] S. K. Kalyankar, Y. H. Lee, and Y. S. Meng, “Two-slope path loss model for curved-tunnel environment with concept of break point,” *IEEE Transactions on Intelligent Transportation Systems*, vol. 21, 2020.
- [28] D. P. Gaillot, E. Tanghe, W. Joseph et al., “Polarization properties of specular and dense multipath components in a large industrial Hall,” *IEEE Transactions on Antennas and Propagation*, vol. 63, no. 7, pp. 3219–3228, 2015.
- [29] D. Dudley, M. Lienard, S. Mahmoud, and P. Degauque, “Wireless propagation in tunnels,” *IEEE Antennas and Propagation Magazine*, vol. 49, no. 2, pp. 11–26, 2007.
- [30] G. J. Foschini and M. J. Gans, “On limits of wireless communications in a fading environment when using multiple antennas,” *Wireless Personal Communications*, vol. 6, no. 3, pp. 311–335, 1998.